Springer

Acta Mechanica Sinica

• RESEARCH PAPER •

Acta Mech. Sin., Vol. 40, 723661 (2024)
https://doi.org/10.1007/s10409-024-23611-x

Micromechanical modelling on the elastoplastic damage and irreversible critical current degradation of the twisted multi-filamentary Nb_3Sn superconducting strand

Ze Jing*, and Yu Zhang

Institute of Extreme Mechanics and School of Aeronautics, Northwestern Polytechnical University, Xi'an 710072, China

Received January 17, 2024; accepted January 31, 2024; published online April 19, 2024

Nb_3Sn is widely accepted as the enabling technology for high field superconducting magnets. However, it is brittle and with strain-sensitive superconducting properties. In high field applications, Nb_3Sn strand experiences significant elastoplastic strain or even damage which causes degradation in its current carrying capacity. In this work, a 3D mean-field homogenization model based on the incremental micromechanics scheme is developed to investigate the elastoplastic damage and irreversible degradation of the twisted multifilamentary Nb_3Sn strand. The effective stress-strain curves and strain distribution in the Nb_3Sn filaments are calculated for the strand under monotonic and cyclic loads. The invariant strain scaling law supplemented with the damage-induced reduction is adopted to characterize the irreversible degradation of the critical current. It is found that twisting plays an important role in elastoplastic damage and strain-induced critical current degradation. With the increasing of twist pitch, the strand becomes stiffer and the strain limit surpasses which the filaments start to damage sharply decreases. Both the accumulated residual strain and damage of the filaments contribute to the irreversible degradation of the critical current. The experimentally observed "strain irreversibility cliff" is the result of damage to the Nb_3Sn filaments. From a mechanical point of view, a short twist pitch will be a good choice to alleviate the strain-induced irreversible degradation of the Nb_3Sn strands.

Superconducting strand, Mean-field homogenization, Incremental micromechanics scheme, Irreversible degradation, Elastoplastic damage, Stress and strain

Citation: Z. Jing, and Y. Zhang, Micromechanical modelling on the elastoplastic damage and irreversible critical current degradation of the twisted multifilamentary Nb_3Sn superconducting strand, Acta Mech. Sin. 40, 723661 (2024), https://doi.org/10.1007/s10409-024-23611-x

1. Introduction

Due to its superior current carrying capacity at the high magnetic field larger than 10 T, Nb_3Sn is widely accepted as the enabling technology for high field superconducting magnets such as the magnets of the international thermonuclear experimental reactor and next generation accelerator [1-4]. However, Nb_3Sn is brittle and its superconducting properties are strain sensitive [5]. In large-scale and high magnetic field applications, the Nb_3Sn conductor experiences significant thermal, mechanical, and electromagnetic stress induced by the thermal contraction and the Lorentz force during cool-down and operation process, which lead to ever-increasing challenges to the application of Nb_3Sn wires [6,7]. Thus, stress/strain measurements and the effects of strain on the superconducting properties have received intense studies during the past few years [8-10].

To alleviate the mechanical brittleness, Nb_3Sn material is usually compounded with bronze matrix to form a composite strand [3,4]. In this process, thousands of Nb_3Sn filaments with a small filament size are embedded into the bronze matrix to circumvent the thermomagnetic instability and fracture. In addition, the Nb_3Sn filaments are twisted into helixes to reduce the time-dependent field-induced AC losses. As has already been reported, the critical current density of the Nb_3Sn superconducting strand depends on the magnetic field, the temperature, and the strain state within

*Corresponding author. E-mail address: zejing@nwpu.edu.cn (Ze Jing)
Executive Editor: Xingzhe Wang

the Nb_3Sn filaments. Historically, extensive strain dependence measurements have been made for the Nb_3Sn strands under applied tension and compression, torsion, and bending strains [11-14]. Based on these measurements, various scaling functions for strain dependence of the Nb_3Sn superconducting strand have been proposed. There is the power-law model developed by Ekin [15], the polynomial function proposed by Taylor and Hampshire [16], the deviatoric strain function by Godeke et al. [17], and the 3-D invariant strain function of Markiewicz [18,19], the semi-phenomenological approach which combines the first-principle calculation and the empirical relation [20]. Among these, the unified scaling law, which is well developed and evaluated by Ekin et al. [21-23], characterizes the full three-dimensional dependences of the critical current on the magnetic field, temperature, and mechanical strain, and is being extensively applied in characterizing the Nb_3Sn strand. Thus, the key issue in developing the strain dependence of the performance of strands is to accurately estimate the internal strain state in the Nb_3Sn filaments.

Despite experimental tests, significant progress has been made to characterize the mechanical behaviours of Nb_3Sn superconducting strands during the past few years. Considering the microstructure of the strands, Boso et al. [24] investigated the effective thermo-mechanical behaviours of the Nb_3Sn superconducting wires using numerical homogenization methods. Chen et al. [25] estimated the local strain in Nb_3Sn filaments by developing a 3D model based on the micromechanics theory. Sun [26] has proposed a multiscale nonlinear procedure to analyse the strain and stress in the Nb_3Sn superconducting accelerator magnets, which can be employed to assess the strain-induced performance degradation of the Nb_3Sn strands. Feng et al. [27] formulated an efficient multiscale nonlinear analysis framework to investigate the mechanical behaviour of Nb_3Sn superconducting accelerator magnet based on a self-consistent clustering method. In these studies, twisting effect of the Nb_3Sn filaments has been ignored which is proven to be an important factor influences the stain distribution in the strand [28].

For the Nb_3Sn strand under axial tension and thermal loading, Ahoranta et al. [29] developed a two-dimensional finite element model to investigate the effect of twisting on the electromechanical properties of Nb_3Sn superconducting strands. Then, we developed a three-dimensional theoretical model based on the micromechanics method to analyse the effect of twisting on the strain distribution and performance degradation of Nb_3Sn strands [30,31]. However, the superconducting properties of the Nb_3Sn strand depend on the strain reversibly up to an irreversible limit where damage occurs in the Nb_3Sn filaments [32-35]. The nonlinear elastoplastic damage behaviours as well as the reversible and irreversible degradation of superconducting properties are not well understood and need effective models to accurately predict and estimate. In 2016, Wang et al. [36,37] developed a finite element model to investigate the effects of residual thermal strain and filament breakage on the mechanical behaviours of the twisted multifilamentary superconducting strand under tensile and cyclic loading. Recently, Jiang et al. [38,39] investigated the quasi-static loading-unloading tensile and fatigue behaviours of the Nb_3Sn superconducting strand through experimental tests and analysis. Nonetheless, the nonlinear elastoplastic and damage behaviour of the composite strand and the irreversible degradation of its superconducting properties are far from fully understood and effective characterization.

In this paper, a mean-field homogenization model based on the incremental micromechanics scheme is proposed to characterize the nonlinear elastoplastic damage behaviour of the Nb_3Sn superconducting strand, and elucidate the mechanism for the reversible and irreversible degradation in the critical current density of Nb_3Sn strand. In the following, Sect. 2 gives a brief introduction to the mean-field homogenization method. In Sect. 3, the elastoplastic constitutive law for the bronze matrix and the isotropic elasticity-based damage model for Nb_3Sn filaments are recalled. The incremental micromechanics scheme is given in Sect. 4. The results and discussions are presented in Sect. 5. The main conclusions are summarized in Sect. 6.

2. Background on the mean-field homogenization method

In this section, the mean-field homogenization formulation [40, 41] based on the Mori-Tanaka method [42] is briefly introduced to approximate the nonlinear elastoplastic damage behaviour of Nb_3Sn superconducting strands. A represent volume element (RVE) can be defined with two phases i.e., the bronze matrix and the Nb_3Sn filaments as inclusions. The Nb_3Sn filaments have a volume fraction of v_I and a stiffness of $\mathbf{C}_I$, while the Bronze matrix has a volume fraction of v_0 and stiffness tensor $\mathbf{C}_0$. In the micromechanics scheme, the average strain $\langle\boldsymbol{\varepsilon}\rangle_I$ in the inclusion is linked with the average strain $\langle\boldsymbol{\varepsilon}\rangle_0$ through the fourth-order local strain concentration tensor $\mathbf{a}_I$ such that [43]

$$\langle\boldsymbol{\varepsilon}\rangle_I = \mathbf{a}_I : \langle\boldsymbol{\varepsilon}\rangle_0. \tag{1}$$

Here, $\mathbf{a}_I$ reflects the microstructure of the composite material and can be expressed as

$$\mathbf{a}_I = \left[\mathbf{I} + \left(\mathbf{S} : \mathbf{C}_0^{-1}\right) : (\mathbf{C}_I - \mathbf{C}_0)\right]^{-1}, \tag{2}$$

in which $\mathbf{I}$ is the fourth-order identity tensor, and $\mathbf{S}$ is the fourth-order Eshelby tensor that depends on $\mathbf{C}_0$ and the shape and orientation of the inclusion. Considering the equal stress condition $v_0\langle \boldsymbol{\varepsilon}\rangle_0 + \sum_{r=1}^{N} v_I \langle \boldsymbol{\varepsilon}\rangle_I = \mathbf{I}$, the average strain in the matrix is related to the applied strain $\bar{\boldsymbol{\varepsilon}}$ as

$$\langle \boldsymbol{\varepsilon}\rangle_0 = \left[v_0 \mathbf{I} + \sum_{I=1}^{N} v_I \mathbf{a}_I \right]^{-1} \bar{\boldsymbol{\varepsilon}}. \tag{3}$$

For the twisted Nb_3Sn filaments, the local strain concentration tensor $\mathbf{a}_I$ is given as follows:

$$\mathbf{a}_I^{\mathrm{TW}} = \left[\mathbf{I} + \mathbf{P}^{\mathrm{TW}} : (\mathbf{C}_I - \mathbf{C}_0) \right]^{-1}, \tag{4}$$

where $\mathbf{P}^{\mathrm{TW}} = \mathbf{S}^{\mathrm{TW}} : \mathbf{C}_0{}^{-1}$, and $\mathbf{S}^{\mathrm{TW}}$ is the modified Eshelby tensor, which can be obtained by the transformation of the Eshelby tensor for ellipsoid from local coordinates to the global coordinates, i.e.,

$$\mathbf{S}^{\mathrm{TW}}_{ijkl} = \mathbf{Q}_{im}\mathbf{Q}_{jn}\mathbf{S}_{mnpq}\mathbf{Q}_{pk}\mathbf{Q}_{ql}. \tag{5}$$

Here, $\mathbf{Q}_{im}$ is the transformation matrix. Considering the symmetry of the Eshelby tensor, it can be written into a matrix and the transformation relationship can be written in the following form:

$$\mathbf{S}^{\mathrm{TW}} = \mathbf{T}\mathbf{S}\mathbf{T}^{-1}, \tag{6}$$

in which $\mathbf{T}$ is the transformation matrix and its specific form can be referred in Refs. [30,41]. Hence, the global concentration tensor for the twisted Nb_3Sn superconducting filaments can be expressed as

$$\mathbf{A}^{\mathrm{TW}} = \left[\mathbf{I} + \mathbf{P}^{\mathrm{TW}} : (\mathbf{C}_I - \mathbf{C}_0) \right]^{-1} : \left[v_0 \mathbf{I} + \sum_{I=1}^{N} v_I \mathbf{a}_I^{\mathrm{TW}} \right]^{-1}. \tag{7}$$

Then, the effective stiffness of the RVE within Mori-Tanaka homogenization can be obtained as follows:

$$\mathbf{C}_{\mathrm{eff}} = \mathbf{C}_0 + \sum_{I=1}^{N} v_I \left[(\mathbf{C}_I - \mathbf{C}_0)^{-1} + v_0 \mathbf{P}^{\mathrm{TW}} \right]^{-1}. \tag{8}$$

3. Constitutive laws for the elastoplastic matrix and brittle filaments

3.1 Nonlinear elastoplastic model for the bronze matrix

3.1.1 Elastoplastic constitutive law

In the superconducting strand, the bronze matrix is an elastoplastic material. During the cool-down and operation of the magnets, significant plastic deformation takes place which induces irreversible degradation of the critical current. In this paper, the J_2 flow theory is adopted to characterize the elastoplastic matrix material. The model can be defined by considering the following equations [44]:

$$\boldsymbol{\sigma} = \mathbf{C}^{\mathrm{el}} : (\boldsymbol{\varepsilon} - \boldsymbol{\varepsilon}^{p}), \tag{9a}$$

$$f = J_2(\boldsymbol{\sigma}) - \sigma_Y - R(p) \le 0, \tag{9b}$$

$$\dot{p} \geqslant 0,\ \dot{p} f = 0,\ p\dot{f} = 0, \tag{9c}$$

$$J_2(\boldsymbol{\sigma}) = \left(\frac{3}{2} \mathbf{s} : \mathbf{s} \right)^{\frac{1}{2}}, \text{ with } \mathbf{s} = \boldsymbol{\sigma} - \frac{1}{3}(\mathrm{tr}\boldsymbol{\sigma})\mathbf{1}, \tag{9d}$$

$$\dot{\boldsymbol{\varepsilon}}^{p} = \dot{p}\mathbf{N}, \text{ with } \dot{p} = \left(\frac{2}{3} \dot{\boldsymbol{\varepsilon}}^{p} : \dot{\boldsymbol{\varepsilon}}^{p} \right)^{\frac{1}{2}}, \tag{9e}$$

$$\mathbf{N} = \frac{\partial f}{\partial \boldsymbol{\sigma}} = \frac{3}{2} \frac{\mathrm{dev}(\boldsymbol{\sigma})}{J_2(\boldsymbol{\sigma})}, \tag{9f}$$

where $\boldsymbol{\sigma}$ is the stress and $\mathbf{C}^{\mathrm{el}}$ is the fourth-order elastic stiffness tensor of the bronze matrix, $\boldsymbol{\varepsilon}$ and $\boldsymbol{\varepsilon}^{p}$ are the total and plastic strains respectively. The yield function f defines the yield surface ($f = 0$) and the elastic domain, in which σ_Y is the initial yield stress, $R(p)$ is the hardening stress and p is the accumulated plastic strain. $\mathbf{N}$ is defined as the vector normal to the yield surface in the stress space, $\mathbf{s}$ is the deviatoric stress, and $\mathbf{1}$ is the second-order symmetric identity tensor.

Following the derivation of Doghri and Ouaar [45], the elastoplastic tangent modulus $\mathbf{C}^{\mathrm{ep}}$ is given as

$$\mathbf{C}^{\mathrm{ep}} = \mathbf{C}^{\mathrm{el}} - \frac{(2G)^2}{h} \mathbf{N} \otimes \mathbf{N},\ h = 3G + \frac{\mathrm{d}R}{\mathrm{d}p}, \tag{10}$$

and the algebraic tangent modulus

$$\mathbf{C}^{\mathrm{alg}} = \mathbf{C}^{\mathrm{ep}} - (2G)^2 \Delta p \frac{J_2(\boldsymbol{\sigma})}{J_2(\boldsymbol{\sigma}^{\mathrm{tr}})} \frac{\partial \mathbf{N}}{\partial \boldsymbol{\sigma}}, \tag{11}$$

in which $\frac{\partial \mathbf{N}}{\partial \boldsymbol{\sigma}} = \frac{1}{J_2(\boldsymbol{\sigma})}\left(\frac{3}{2}\mathbf{I}^{\mathrm{dev}} - \mathbf{N} \otimes \mathbf{N} \right)$, and G is the shear modulus, $\boldsymbol{\sigma}^{\mathrm{tr}}$ is the trial stress, and $\mathbf{I}^{\mathrm{dev}}$ is the deviatoric part of the fourth-order identity tensor.

3.1.2 Return mapping algorithm for the internal variables

The main problem in modelling plastic deformation is to find the internal variables $\left(p_{n+1}, \boldsymbol{\varepsilon}^{p}_{n+1}\right)$ at t_{n+1} from the previous state $\left(p_n, \boldsymbol{\varepsilon}^{p}_{n}\right)$ at t_n. Detailed numerical procedures are as follows.

Given the increment of total strain $\Delta\boldsymbol{\varepsilon}$ and the internal variables at t_n, calculate elastic predictor at t_{n+1}

$$\boldsymbol{\sigma}^{\mathrm{tr}}_{n+1} = \mathbf{C}^{\mathrm{el}} : \left(\boldsymbol{\varepsilon}_{n+1} - \boldsymbol{\varepsilon}^{p}_{n} \right), \tag{12}$$

$$\boldsymbol{\varepsilon}^{p}_{n+1} = \boldsymbol{\varepsilon}^{p}_{n}. \tag{13}$$

If $f \le 0$, the stress state is inside the trial yield surface, which means the elastic trail state is the solution

$$\boldsymbol{\sigma}_{n+1} = \boldsymbol{\sigma}^{\mathrm{tr}}_{n+1}, \tag{14}$$

$$\left(p_{n+1}, \boldsymbol{\varepsilon}^{p}_{n+1}\right) = \left(p_n, \boldsymbol{\varepsilon}^{p}_{n}\right). \tag{15}$$

Else if $f > 0$, the equivalent trial stress is larger than the yield stress, and a correction should be made to find a stress state $\boldsymbol{\sigma}_{n+1}$ that satisfies $f = 0$. Here, the Newton-Raphson method is adopted to find the internal variables by solving the following equations:

$$\mathbf{k}_{\tilde{\mathbf{s}}} \equiv \mathbf{s} - \mathbf{s}^{\mathrm{tr}} + 2G_0\mathbf{N}\Delta p = \mathbf{0}, \tag{16}$$

$$f \equiv J_2\left(\boldsymbol{\sigma}_{n+1}^{\mathrm{tr}}\right) - R(p + \Delta p) - \sigma_Y = 0. \tag{17}$$

Then the internal variables can be updated for the next steps.

3.2 Isotropic elasticity-based damage model for Nb_3Sn filaments

The mechanical failure of the Nb_3Sn filaments is modelled in the spirit of continuum damage mechanics [46,47] in which the amount of deterioration due to crack growth is represented by a state variable D such as $(0 \le D < 1)$. This damage variable controls the degradation of the material and leads to nonlinearity in the constitutive law. Here, the concept of effective stress $\hat{\boldsymbol{\sigma}}$ which is thought to work on the undamaged filament is introduced as

$$\hat{\boldsymbol{\sigma}} = \frac{\boldsymbol{\sigma}}{1 - D}, \tag{18}$$

where $\boldsymbol{\sigma}$ is the damaged stress tensor accounting for the damage evolution. Then, the degraded stiffness tensor $\mathbf{C}^{\mathrm{d}}$ during the damage process can be given as

$$\mathbf{C}^{\mathrm{d}} = (1 - D)\mathbf{C}^{\mathrm{el}}. \tag{19}$$

For the elasticity-based damage model, the above relations are supplemented by a damage loading function $g(\boldsymbol{\varepsilon}_{\mathrm{eq}}, \kappa)$, which is written as

$$g = \boldsymbol{\varepsilon}_{\mathrm{eq}} - \kappa \le 0, \tag{20}$$

with κ the internal variable and $\boldsymbol{\varepsilon}_{\mathrm{eq}}$ the scalar function of the strain tensors. The evolution of the internal variable during the loading-unloading process follows the Karush-Kuhn-Tucker conditions [47]:

$$g \le 0,\ \dot{\kappa} \geqslant 0,\ \text{and}\ \dot{\kappa}g = 0, \tag{21}$$

which can be solved using a similar procedure in Sect. 3.1.2.

To characterize the mechanical behaviors of brittle Nb_3Sn filaments, the definition of the equivalent strain $\boldsymbol{\varepsilon}_{\mathrm{eq}}$ is chosen as suggested by Mazars and Pijaudier-Cabot [46]

$$\boldsymbol{\varepsilon}_{\mathrm{eq}} = \sqrt{\sum_{i=1}^{3} \langle \boldsymbol{\varepsilon}_i \rangle^2}, \tag{22}$$

with $\boldsymbol{\varepsilon}_i$ the principal strain, and $\langle \cdot \rangle$ the MacAulay brackets defined as $\langle \boldsymbol{\varepsilon}_i \rangle = \boldsymbol{\varepsilon}_i$ if $\boldsymbol{\varepsilon}_i > 0$ and $\langle \boldsymbol{\varepsilon}_i \rangle = 0$ otherwise. The damage evolution law is taken as

$$D(\kappa) = \begin{cases} 1 - \dfrac{\boldsymbol{\varepsilon}_0}{\kappa}\exp\left(-\dfrac{\kappa - \boldsymbol{\varepsilon}_0}{\boldsymbol{\varepsilon}_f - \boldsymbol{\varepsilon}_0}\right), & \kappa \geqslant \boldsymbol{\varepsilon}_0, \\ 0, & \kappa < \boldsymbol{\varepsilon}_0, \end{cases} \tag{23}$$

in which $\boldsymbol{\varepsilon}_0$ is the strain limit where the damage occurs, which can be obtained from the tensile strength σ_{ts} and Young's modulus E_0. While, $\boldsymbol{\varepsilon}_f$ is a material parameter which controls when the material is fully damaged. Hence, the algebraic tangent modulus of the brittle filaments after damage can be expressed as

$$\mathbf{C}^{\mathrm{alg}} = (1 - D)\mathbf{C}^{\mathrm{el}} - \frac{\partial D}{\partial \kappa}\frac{\partial \kappa}{\partial \boldsymbol{\varepsilon}_{\mathrm{eq}}}\left(\mathbf{C}^{\mathrm{el}} : \boldsymbol{\varepsilon}\right) \otimes \frac{\partial \boldsymbol{\varepsilon}_{\mathrm{eq}}}{\partial \boldsymbol{\varepsilon}}. \tag{24}$$

4. Numerical homogenization scheme and procedures

4.1 Incremental micromechanics scheme (IMS)

In this section, the basics of the incremental micromechanics scheme [48, 49] will be briefly provided. For the Nb_3Sn superconducting strand, it is conceived as a composite with hundreds of twisted filaments embedded into the bronze matrix. Shown in Fig. 1(a) and (b) are the three-dimensional configuration and cross-sectional view of a typical re-stacked-rod-process (RRP) Nb_3Sn strand which we consider in the following calculations. The twisted Nb_3Sn filaments are classified into different layers according to their helical radius. For the RRP strand, we group the filaments into 12 layers as shown in Fig. 1(c), and filaments in the same layer have the same helical radius. Table 1 presents the typical geometry parameters of the twisted filaments [50], which are adopted in the following simulations. The representative volume element (RVE) we take is a cylinder with a radius of R and height L, as illustrated in Fig. 2. In the RVE, each filament is considered a helix with a helical angle α_{0i}, helical radius R_{0i}, and pitch length $p_0(= L)$. The IMS scheme is based on the differential scheme in which the composite is assumed to be made of gradual addition of infinitesimal reinforcements into the matrix. In the numerical homogenization process, the filaments are divided into infinitesimal long-ellipsoids along the central axis of the helix (as illustrated in Fig. 2(b)). The effective properties of the Nb_3Sn superconducting strand are obtained by the gradual addition of the long-ellipsoids into the bronze matrix as shown in Fig. 2(c). At each step, the infinitesimal long-

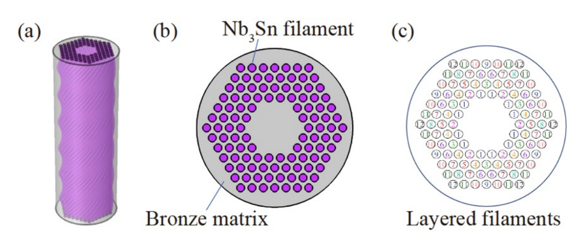

Figure 1 (a) Three dimensional configuration of the Nb_3Sn strand; (b) cross sectional view of the Nb_3Sn composite strand; (c) layer number of the Nb_3Sn filaments in the composite strand.

Table 1 Geometrical parameters for the filaments in the RRP Nb_3Sn strand [50]

Layer	Number of filaments	Helical radius (mm)
1	12	0.135
2	6	0.15
3	6	0.175
4	12	0.185
5	6	0.205
6	12	0.22
7	12	0.23
8	6	0.255
9	6	0.265
10	12	0.27
11	12	0.285
12	6	0.305

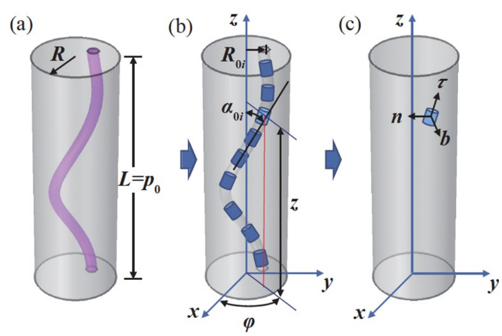

Figure 2 (a) Single Nb_3Sn filaments in the strand; (b) discretized filaments; (c) RVE of the inclusion problem.

ellipsoid is added to the matrix followed by a homogenization process to obtain the effective properties. The homogenized composite at step n is considered as matrix at step $n+1$, new ellipsoids are injected into the matrix followed by a homogenization process, and then step forward until the elements of all filaments are injected into the matrix.

Based on the incremental homogenization scheme, the numerical procedures for the mean-field homogenization of the elastoplastic damage behaviour of Nb_3Sn superconducting strands adopted in this paper are presented as follows:

(1) Initialization: given the strain $\bar{\boldsymbol{\varepsilon}}_n$ and macroscopic strain increment $\Delta\bar{\boldsymbol{\varepsilon}}$, $\bar{\boldsymbol{\sigma}}_n$, p_n, κ_n, and D_n at the step n.

(2) Start the IMS scheme with an initial global concentration tensor $\mathbf{A}^{\mathrm{TW}} = \mathbf{I}$, and compute the strain increment in the matrix phase: $\Delta\boldsymbol{\varepsilon}^0 = \mathbf{A}^{\mathrm{TW}} : \Delta\bar{\boldsymbol{\varepsilon}}$.

(a) Update the stress in the matrix phase from Eq. (9);

(b) Compute the algorithmic moduli $\mathbf{C}_0^{\mathrm{alg}}$ of the matrix from Eq. (11).

(3) Compute the strain increment in the inclusion phase: $\Delta\boldsymbol{\varepsilon}^I = \dfrac{\Delta\bar{\boldsymbol{\varepsilon}} - v_0\Delta\boldsymbol{\varepsilon}^0}{\sum_{I=1}^N v_I}$.

(a) Update the stress in the inclusion phase from Eq. (18);

(b) Compute the algorithmic moduli $\mathbf{C}_I^{\mathrm{alg}}$ of the inclusion from Eq. (24).

(4) Apply the mid-point rule to the algorithmic moduli of inclusion and matrix:

$$\left(\mathbf{C}_0^{\mathrm{alg}}\right)_{n+\alpha} = (1-\alpha)\left(\mathbf{C}_0^{\mathrm{alg}}\right)_n + \alpha\mathbf{C}_0^{\mathrm{alg}}, \tag{25}$$

$$\left(\mathbf{C}_I^{\mathrm{alg}}\right)_{n+\alpha} = (1-\alpha)\left(\mathbf{C}_I^{\mathrm{alg}}\right)_n + \alpha\mathbf{C}_I^{\mathrm{alg}}. \tag{26}$$

Here, $\alpha \in [0,1]$ is a parameter for numerical stabilization.

(5) Compute the global concentration tensor $\mathbf{A}^{\mathrm{TW}}$ from Eq. (7) using the IMS scheme.

(6) Check whether $\mathbf{A}^{\mathrm{TW}}$ satisfy the residual error tolerance: $R = |\mathbf{A}^{\mathrm{TW}} : \Delta\bar{\boldsymbol{\varepsilon}} - \Delta\boldsymbol{\varepsilon}^0| < \mathrm{TOL}$. In the following simulations, we take the tolerance value $\mathrm{TOL} = 10^{-9}$. If the error is tolerable, then exit the loop and go to step 7; if it is not, go to step 2 with the updated global strain concentration tensor $\mathbf{A}^{\mathrm{TW}}$.

(7) Calculate the homogenized tangent moduli $\mathbf{C}_{\mathrm{eff}}$ using Eq. (8), and compute the stress increment $\Delta\boldsymbol{\Sigma} = \mathbf{C}_{\mathrm{eff}} : \Delta\bar{\boldsymbol{\varepsilon}}$.

(8) Update the macroscopic stress for the next step, $\bar{\boldsymbol{\sigma}}_{n+1} = \bar{\boldsymbol{\sigma}}_n + \Delta\bar{\boldsymbol{\sigma}}$, $\bar{\boldsymbol{\varepsilon}}_{n+1} = \bar{\boldsymbol{\varepsilon}}_n + \Delta\bar{\boldsymbol{\varepsilon}}$.

4.2 Strain dependence of the critical current density

The critical current density of the Nb_3Sn superconductor depends on the strain reversibly up to the strain limit of the material. While the critical current density degrades irreversibly when damage or cracks occur in Nb_3Sn under excessive strain and stress. In this work, the invariant strain scaling law based on the flux pinning is adopted to characterize the reversible critical current density degradation of the Nb_3Sn superconductor. The strain dependences of the critical temperature and the upper critical magnetic field are given by [18,19]

$$\frac{T_c^*(\boldsymbol{\varepsilon})}{T_c^*(0)} \approx \frac{1}{1+a_1 I_1}, \tag{27}$$

$$\frac{B_{c2}^*(\boldsymbol{\varepsilon})}{B_{c2}^*(0)} = \frac{1}{(1+a_1 I_1)\left(1+a_2 J_2 + a_3 J_3 + a_4 J_2^2\right)}, \tag{28}$$

in which a_1, a_2, a_3, and a_4 are material dependent parameters, the values of which are taken from Refs. [18,19] with $a_1 = -2.3$, $a_2 = 4.63 \times 10^3$, $a_3 = 6.54 \times 10^5$, and $a_4 = 3.4 \times 10^6$. I_1, J_2, and J_3 are the first, second, and third strain invariants respectively. Hence, the strain dependence of the critical current density can be expressed as [21-23]

$$J_c = A(\boldsymbol{\varepsilon})\left[T_c^*(\boldsymbol{\varepsilon})\left(1-t^2\right)\right]^2 \left[B_{c2}^*(T,\boldsymbol{\varepsilon})\right]^{n-3} b^{p-1}(1-b)^q, \tag{29}$$

where $A\left(\boldsymbol{\varepsilon}\right) = A_0\left[T_c^*\left(\boldsymbol{\varepsilon}\right)/T_c^*(0)\right]^s$, $B_{c2}^*(T,\boldsymbol{\varepsilon}) = B_{c2}^*(\boldsymbol{\varepsilon})(1-t^v)$, $t = T/T_c^*(\boldsymbol{\varepsilon})$, $b = B/B_{c2}^*(T,\boldsymbol{\varepsilon})$, and the values of material dependent parameters A_0, $T_c^*(0)$, $B_{c2}^*(0)$, s, v, n, p, and q are given as in Table 2.

Furthermore, when the strain in the filaments exceeds the strain limit of the Nb_3Sn material the critical current degrades irreversibly. Here, a damage-related term is proposed to take this effect into account, i.e.,

$$J_c(B,T,\boldsymbol{\varepsilon},D) = J_c(B,T,\boldsymbol{\varepsilon})(1-D)^{\beta}, \tag{30}$$

in which β is a material-dependent parameter, and we take it 0.5 in the following calculations.

5. Results and discussions

In this section, the mean-field homogenization method based on the IMS has been used to characterize the mechanical behaviour and the strain-induced critical current degradation of the Nb_3Sn strand. The diameter of the strand is taken to be $R = 0.7$ mm, pitch length $p_0 = 12$ mm [50]. Other geometry parameters are also taken from Ref. [50] for the Nb_3Sn strand produced by Oxford superconducting technology (OST) with RRP. The Nb_3Sn filament is considered isotropic and elastic-brittle with Young's modulus $E_I = 100$ GPa, Poisson's ratio $\vartheta_I = 0.3$, strain limit $\boldsymbol{\varepsilon}_0 = 0.24\%$, and $\boldsymbol{\varepsilon}_f = 0.33\%$ [5]. The bronze matrix is elastoplastic with Young's modulus $E_0 = 137$ GPa, Poisson's ratio $\vartheta_0 = 0.34$, and a power-law isotropic hardening law $R(p) = kp^m$ (here, we take $k = 383.63$ MPa and $m = 0.2859$) [51]. In the following calculations, two cases are considered: the nonlinear elastoplastic behaviour of the strand without considering the damage of Nb_3Sn filaments, and the elastoplastic damage behaviour of the Nb_3Sn strand. The main results and discussions are presented as follows.

5.1 Nonlinear elastoplastic behaviour of the strand: without damage

Figure 3 presents the effective axial stress-strain curves of the Nb_3Sn strand subjected to an axial tensile load monotonically increasing from the free state. The predicted results are compared with experimental measurements on the Nb_3Sn strand with RRP [13,14]. It can be seen that the effective stress-strain of the composite strand shows typical elastoplastic characteristics and the numerical homogenization results are in good agreement with the experimental results of Ref. [13]. The results demonstrate that the micromechanics model and the nonlinear mean-field homogenization scheme developed in this work are capable of characterizing the effective elastoplastic behavior of the twisted multifilamentary Nb_3Sn strands. It is also to be noted that there are non-negligible differences between the numerical results and the experimental results of the OST strand from Ref. [14]. This discrepancy may be originated from the differences between the material parameters we chose in the simulation and the real mechanical properties of the Nb_3Sn and bronze materials. In addition, other phases in the composite strand such as the intermetallic alloys and voids introduced during the manufacturing process of the Nb_3Sn strand are also neglected in our simulation.

The elastoplastic strain in the strand when subjected to cyclic loads plays a crucial role in the irreversible degradation of the critical current. To investigate the cyclic elastoplastic behaviour, a cyclic axial tensile stress as shown in Fig. 4(a) is applied to the strand. Figure 4(b) shows the average stress-strain curves of the composite strand, the filaments, and the matrix represented by the solid, the dash-dotted, and short-dotted lines respectively. From the cyclic stress-strain response, it can be found that the Nb_3Sn filaments behave elastically with a linear stress-strain relationship, while the bronze matrix demonstrates typical nonlinear-elastoplastic characteristics. The stress-strain curves reveal that the strand yields at the very beginning of the loading. Moreover, residual strains accumulate in the Nb_3Sn strand as the cyclic load continues. Although the Nb_3Sn material is linear-elastic, residual strain accumulated due to the plastic deformation of the bronze matrix as the load exceeds the elastic limit released. This explains why the Nb_3Sn strand shows an irreversible degradation in the critical current even if the load does not exceed the strain limit. In Fig. 4(c), the residual strain distributions in the Nb_3Sn filaments when the load is released are presented. As can be seen, strain in the Nb_3Sn filament does not vary along the

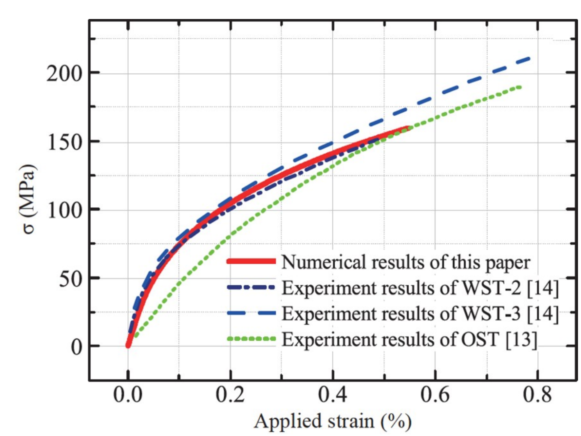

Figure 3 Elastoplastic stress-strain curve of the Nb_3Sn strand subjected to the monotonically increasing axial tensile load.

Table 2 Materials parameters for the strain scaling law [16]

A_0 $(\mathrm{A\,m^{-2}\,T^{3-n}\,K^{-2}})$	$T_c^*(0)$ (K)	$B_{c2}^*(0)$ (T)	s	v	n	p	q
9.46×10^6	17.58	29.59	1.0	1.5	2.457	0.5	2.0

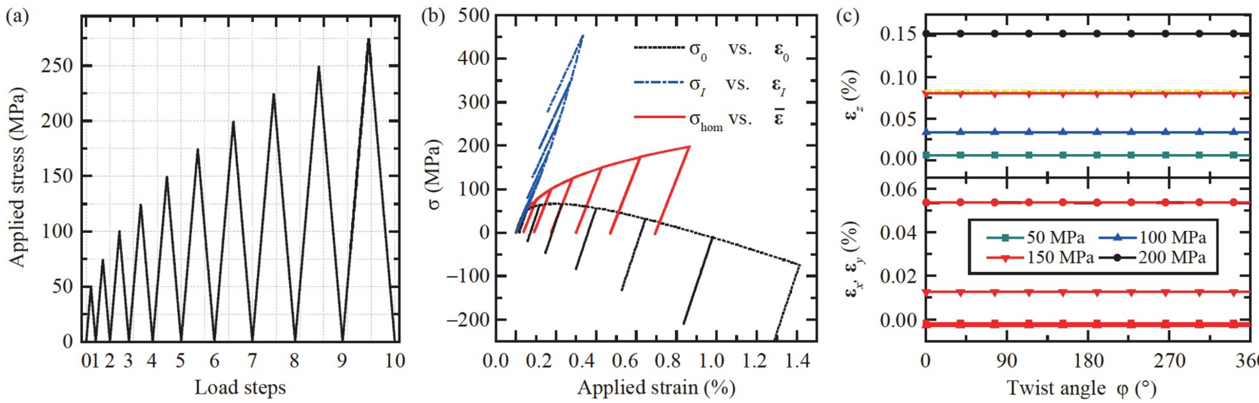

Figure 4 (a) Cyclic tensile stress applied to the Nb_3Sn strand; (b) average stress-strain curve of the Nb_3Sn strand, the filaments, and the matrix; (c) residual strain distribution in the Nb_3Sn filaments when the load is released.

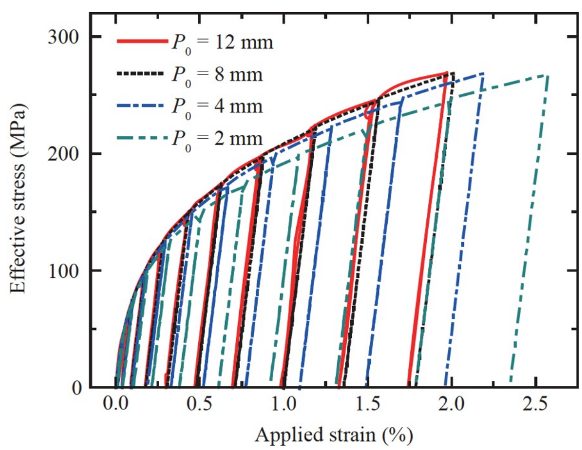

Figure 5 Stress-strain along the axial direction of the Nb_3Sn strand subjected to cyclic tensile load, for the twisted strand with different pitch lengths.

length of the strand. This is consistent with the conclusion made in Ref. [29] that when the ratio of the twist pitch to the helical radius of the outermost filament is larger than 25, the twisting effect can be ignored. For the strand we modelled here, the ratio is about 40. From Fig. 4(c), it is seen that when the applied axial stress is smaller than 50 MPa residual strain in the Nb_3Sn filaments is negligible. As the magnitude of the cyclic stress increases, the residual strain in the filament becomes prominent.

In addition, the twisting effects on the cyclic elastoplastic behaviour of the Nb_3Sn strand are numerically simulated. As demonstrated in Fig. 5, under the same strain the effective stress along the axial direction of the strand increases with the increasing of the twist pitch. This is consistent with the fact that the twisted filaments transit from helical springs to straight lines as the twist pitch increases. Thus, the composite strand becomes stiffer as the twist pitch increases. Similar results have also been reported from experimental measurements on the untwisted and twisted strands (see Fig. 3 in Ref. [28]). In Fig. 6, the strain distribution in the Nb_3Sn filaments of the strand with different pitch lengths is de-

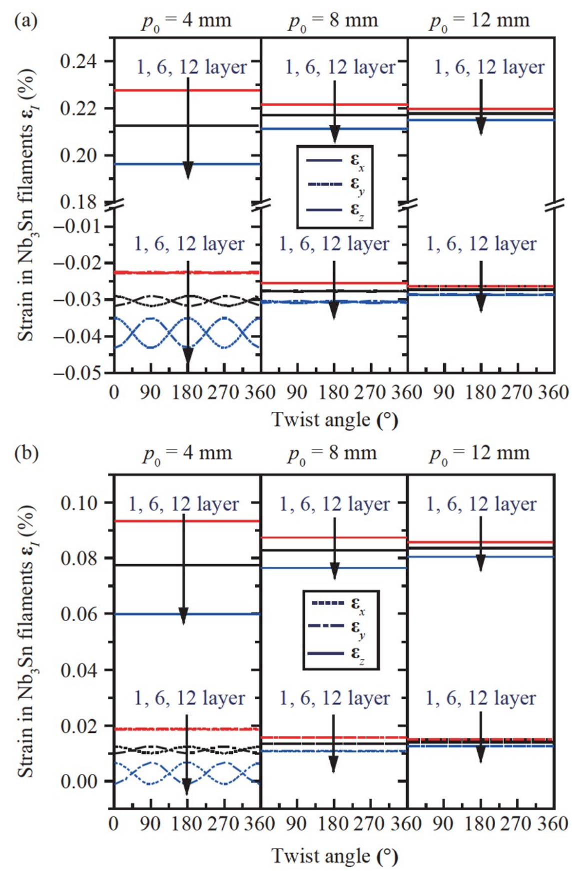

Figure 6 (a) Strain distribution in the Nb_3Sn filaments at different layers when the load is cyclically increased to 150 MPa as shown in Fig. 4(a); (b) remanent strain distribution in the Nb_3Sn filament when the load is released to zero after reaching 150 MPa.

monstrated. Figure 6(a) and (b) show the strain distribution in the Nb_3Sn filaments at different layers when the load is cyclically increased to 150 MPa and released to zero. As expected, variation of the strain with the length of the filaments becomes significant as the pitch length of the twisted strand decreases. In general, variation in the outermost filaments is more evident than the interior filaments because of their larger twist angle. It is also found that the difference in the strain state of the filaments within different layers gets significant when the twist pitch decreases.

5.2 Elastoplastic damage behaviour of the Nb_3Sn strand

In Sect. 5.1, mechanical failure of the Nb_3Sn filaments is not considered. In this section, the elastoplastic damage behaviour of the Nb_3Sn strand is formulated based on the elastoplastic model of the bronze matrix and the isotropic elasticity-based damage model of the filaments.

The numerical results of the Nb_3Sn strand subjected to a monotonically increasing axial tension are presented in Figs. 7 and 8. Figure 7(a) and (b) show the stress-strain curves, the overall damage, and the degradation of the critical current of the strand. As can be seen from Fig. 7(a), damage occurs in the Nb_3Sn filaments when the macro-strain of the strand is about 0.5%. After reaching its maximum, the stress in the filament sharply decreases as damage evolves with the increasing load. These results are consensus with our settings of the elasticity-based damage model with the initiation strain $\varepsilon_0 = 0.24\%$ and an exponential damage evolution law. If the tensile load continues to increase, the stress in the filaments decreases exponentially until full damage occurs. During this process, there is a transition from the state that the stress is undertaken by both the filaments and matrix to that the stress is undertaken by the matrix. The homogenized stress-strain curve demonstrates this feature and manifests a "platform" when the filaments are fully damaged. From the damage evolution and the critical current degradation curves shown in Fig. 7(b), we can conclude that the critical current is degraded by the intrinsic strain in the filaments within the strain limit. While damage occurs in the filaments, the critical current degrades sharply with the increase of strain, which is a reproduction of the so-called "strain irreversibility cliff" phenomena found in experiments [35]. In Fig. 8, the damage evolution of the Nb_3Sn filaments within the composite strand subjected to tensile loads is presented. It is seen that all the first filaments (with initial twist angle $\varphi = 0$) in the strand start to break around the locations where the phase angle $\varphi = 90°$ and $180°$. As the tensile load further increases, the damaged region spreads out to the whole filaments. In addition, it can also be inferred that the outer layer filaments are damaged more severely during the tensile loading process.

To have a good understanding of the twisting effects, Nb_3Sn strands with different twist pitches under monotonically increasing tensile load have been simulated. Figure 9(a) shows the effective stress-strain curves of the twisted Nb_3Sn strands with different pitch lengths. Comparing the stress-strain curves, it is found that the initiation point of the

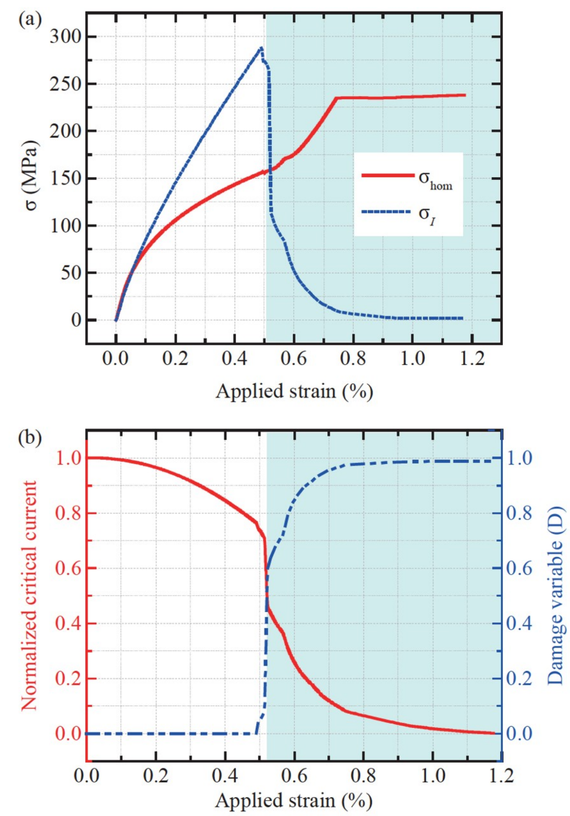

Figure 7 (a) Average stress in the axial direction of the Nb_3Sn strand and the filaments; (b) overall damage and normalized critical current degradation of the Nb_3Sn strand subjected to a monotonic axial tensile load when considering the damage of Nb_3Sn filaments.

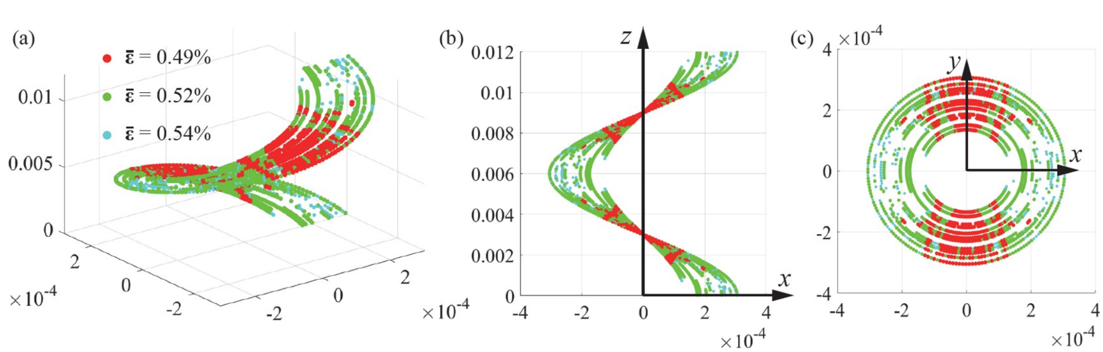

Figure 8 Damage evolution of the Nb_3Sn filaments during the tensile loading process: (a) isometric; (b) side; (c) vertical view of the damage distribution along the filaments.

mechanical failure for the Nb_3Sn strands decreases with the increase of the pitch length. For the strand with a pitch length of 2 mm, the filaments damage until the overall strain in the strand reaches about 1.08%. As the pitch length increases, the strain limit of the twisted strand that damage occurs decreases exponentially (see Fig. 9(b)). This can be interpreted that when the pitch length increases, the twisted filaments behaves more like straight cylinders, the strand becomes stiffer and the effective strain in the filaments exponentially increases under the same axial tensile load. In addition, we have also investigated the twisting effects on the degradation of the critical current. As illustrated in Fig. 9 (c), all the strands show a sharp decrease in the critical current density as damage occurs in the filament. The more severely the filament is twisted in the strand manufacturing process, the higher the irreversible strain limit of the critical current degradation. Furthermore, the "strain irreversibility cliff" effect becomes more pronounced when the pitch length of the twisted filaments increases. From a mechanical point of view, short twist pitch will benefit the alleviation of the strain-induced irreversible degradation of the critical current of the Nb_3Sn strand.

Last but not least, the elastoplastic damage behaviours of the Nb_3Sn strand subjected to the cyclic tensile load are also investigated. Figure 10(a)-(c) demonstrate the stress-strain curve, the overall damage evolution, and the degradation of critical current respectively. From Fig. 10(a), we can see that under the cyclic load, the residual strain accumulated in the strand is the same as that shown in Fig. 4(b) until the damage occurred at the strain as indicated by the solid dots. The correlated overall damage evolution in the filaments is shown in Fig. 10(b). It is clearly seen that the damage initiates when the average strain in the strand reaches about 0.49%. Then, the damage sharply increases as the load increases until the turning point, after which the damage remains the same as the load decreases. As the load increases once again, the damage increases, and more parts of the filaments break. The inset images show the damage distribution in the filaments correlated with the coloured dots on the overall damage evolution curve. More importantly, the critical current density of the strand under the cyclic tensile stress is presented in Fig. 10(c). The solid and open circles with unprimed and primed letters indicate the corresponding "loaded" and "unloaded" points shown in Fig. 10(a). It shows that the critical current degrades irreversibly with a negligible magnitude from the beginning of the

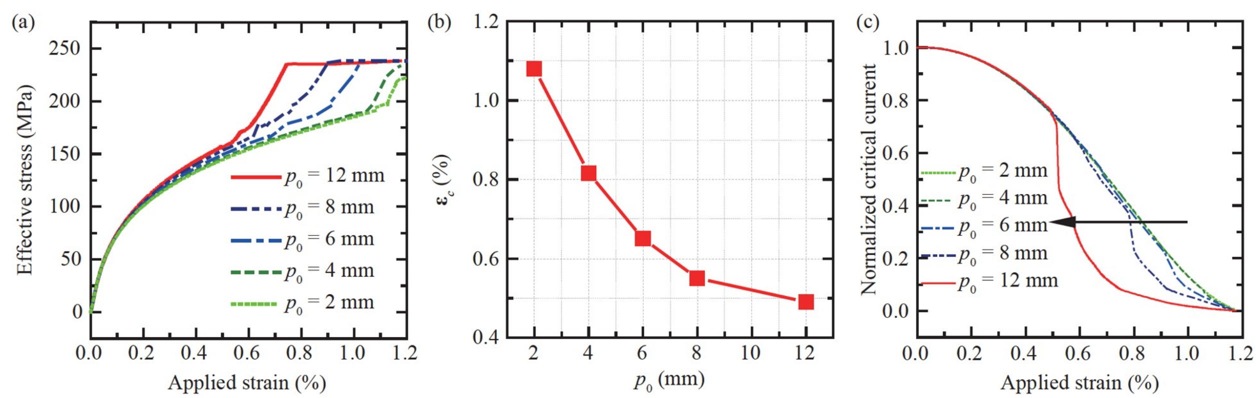

Figure 9 (a) Average stress-strain curve along the axial direction of the strand subjected to a monotonic axial tensile load when considering the damage of Nb_3Sn filaments; (b) tensile strain limit of the strand as a function of pitch length; (c) critical current degradation of the Nb_3Sn strands with different pitch lengths.

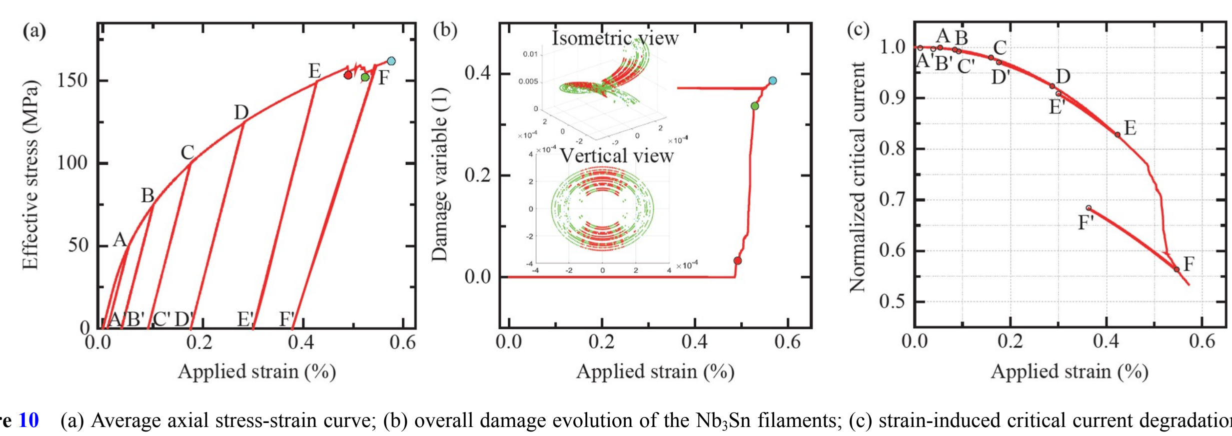

Figure 10 (a) Average axial stress-strain curve; (b) overall damage evolution of the Nb_3Sn filaments; (c) strain-induced critical current degradation of the Nb_3Sn strand when subjected to a cyclic tensile load.

loading process (see points A and A′, B and B′). As the magnitude of the cyclic load gets larger, the irreversibility in the degradation of the critical current becomes significant. If the cyclic loading process continues, more pronounced irreversible degradation occurs. When the strain in the filaments reaches the strain limit, the strain "irreversibility cliff" occurs in the strain-induced current degradation curve. As indicated by the loaded and unloaded points F and F′ in the degradation curve, more pronounced irreversible degradation of the critical current can be found when the filaments are cracked.

Moreover, the twisting effects on the cyclic elastoplastic damage behaviour of the Nb_3Sn strand are also evaluated. Figure 11 shows the axial stress-strain curves of the twisted Nb_3Sn strands with different pitch lengths. It demonstrates that the Nb_3Sn strands with a larger pitch length are stiffer than those with a shorter pitch length. Similar to the monotonic loading cases, the strain limit of the twisted strand after which the filaments are damaged sharply decreases. When the ratio of the twist pitch p_0 to the helical radius gets large enough, the effective strain limit of the strand almost remains constant.

6. Conclusions

In conclusion, a 3D mean-field homogenization model based on the incremental micromechanics scheme is developed to investigate the elastoplastic damage and irreversible critical current degradation of the twisted multifilamentary Nb_3Sn superconducting strand. The effective stress-strain curves as well as the strain distribution in the Nb_3Sn filaments are calculated for the strand under monotonic and cyclic tensile loads respectively. The invariant strain scaling law supplemented with the proposed damage-related factor is adopted to characterize the irreversible degradation of the critical current of the Nb_3Sn strand. In addition, the effects of twisting on the elastoplastic damage and current density degradation of the strand are discussed in detail.

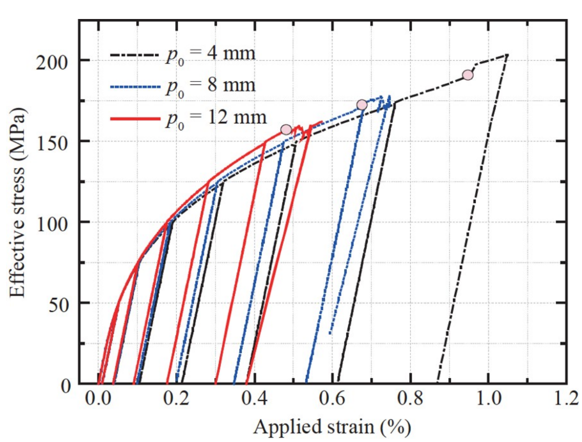

Figure 11 Axial stress-strain curves of the twisted Nb_3Sn strands with different pitch lengths, when subjected to cyclic tensile loads.

It is found that the twist of the strand plays an important role in the elastoplastic damage behaviour and strain dependence of the critical current. With the increase of the twist pitch length, the composite strand becomes stiffer and the strain limit that the filaments starts to damage decreases exponentially. Both the accumulated residual strain in the Nb_3Sn filaments due to the plastic deformation of the bronze matrix and the damage of the filaments when the strain exceeds the strain limit contribute to the irreversible degradation of the critical current of the Nb_3Sn strands. The experimentally observed "strain irreversibility cliff" effect is the result of the damage of the Nb_3Sn filaments which becomes more pronounced as the pitch length increases. From a mechanical point of view, a short twist pitch will be a good choice to alleviate the strain-induced irreversible degradation of the critical current of Nb_3Sn strands. The calculated results demonstrate that the mean-field homogenization model and the numerical scheme proposed in this work are reasonable and effective in characterizing the cyclic elastoplastic damage behaviour and the critical current degradation of the twisted Nb_3Sn superconducting strand.

Conflict of interest *On behalf of all authors, the corresponding author states that there is no conflict of interest.*

Author contributions *Ze Jing designed the model and the computational framework of this study, made numerical simulations, and wrote and edited the manuscript. Yu Zhang collected experimental data and aided in preparing the figures and tables.*

Acknowledgements *This work was supported by the National Natural Science Foundation of China (Grant Nos. 11602185, 11972271, and 12322208), the Young Elite Scientists Sponsorship Program by CAST (Grant No. 2020QNRC001), and the Fundamental Research Funds for the Central Universities.*

1 A. den Ouden, S. Wessel, E. Krooshoop, and H. ten Kate, Application of Nb_3Sn superconductors in high-field accelerator magnets, IEEE Trans. Appl. Supercond. **7**, 733 (1997).
2 D. Ciazynski, Review of Nb_3Sn conductors for ITER, Fusion Eng. Des. **82**, 488 (2007).
3 X. Xu, A review and prospects for Nb_3Sn superconductor development, Supercond. Sci. Technol. **30**, 093001 (2017).
4 R. G. Sharma, Superconductivity: Basics and Applications to Magnets (Springer International Publishing, Cham, 2015).
5 M. T. Dylla, S. E. Schultz, and M. C. Jewell, Fracture strength distribution of individual Nb_3Sn filaments, IEEE Trans. Appl. Supercond. **26**, 1 (2016).
6 A. Devred, I. Backbier, D. Bessette, G. Bevillard, M. Gardner, C. Jong, F. Lillaz, N. Mitchell, G. Romano, and A. Vostner, Challenges and status of ITER conductor production, Supercond. Sci. Technol. **27**, 044001 (2014).
7 N. Mitchell, M. Breschi, and V. Tronza, The use of Nb_3 Sn in fusion: Lessons learned from the ITER production including options for management of performance degradation, Supercond. Sci. Technol. **33**, 054007 (2020).
8 X. J. Zheng, Preface: Mechanical perturbations induced quench: A

challenge of superconductor mechanics. Natl. Sci. Rev. **10**, nwad044 (2023).
9 Y. H. Zhou, D. Park, and Y. Iwasa, Review of progress and challenges of key mechanical issues in high-field superconducting magnets, Natl. Sci. Rev. **10**, nwad001 (2023).
10 X. Zhang, and J. Qin, Mechanical effects: Challenges for high-field superconducting magnets, Natl. Sci. Rev. **10**, nwac220 (2023).
11 A. Nijhuis, R. P. Pompe van Meerdervoort, H. J. G. Krooshoop, W. A. J. Wessel, C. Zhou, G. Rolando, C. Sanabria, P. J. Lee, D. C. Larbalestier, A. Devred, A. Vostner, N. Mitchell, Y. Takahashi, Y. Nabara, T. Boutboul, V. Tronza, S. H. Park, and W. Yu, The effect of axial and transverse loading on the transport properties of ITER Nb_3Sn strands, Supercond. Sci. Technol. **26**, 084004 (2013).
12 A. Nijhuis, Y. Ilyin, S. Wessel, E. Krooshoop, L.Feng, and Y. Miyoshi, Summary of ITER TF Nb_3Sn strand testing under axial strain, spatial periodic bending and contact stress, IEEE Trans. Appl. Supercond. **19**, 1516 (2009).
13 L. Muzzi, V. Corato, A. della Corte, G. De Marzi, T. Spina, J. Daniels, M. Di Michiel, F. Buta, G. Mondonico, B. Seeber, R. Flükiger, and C. Senatore, Direct observation of Nb_3Sn lattice deformation by high-energy x-ray diffraction in internal-tin wires subject to mechanical loads at 4.2 K, Supercond. Sci. Technol. **25**, 054006 (2012).
14 F. Shen, H. Zhang, C. Huang, and L. Li, Experimental study on strain sensitivity of internal-Tin Nb_3Sn superconducting strand based on non-destructive technology, Physica C **584**, 1353784 (2021).
15 J. W. Ekin, Strain scaling law for flux pinning in practical superconductors. Part 1: Basic relationship and application to Nb_3Sn conductors, Cryogenics **20**, 611 (1980).
16 D. M. J. Taylor, and D. P. Hampshire, The scaling law for the strain dependence of the critical current density in Nb_3Sn superconducting wires, Supercond. Sci. Technol. **18**, S241 (2005).
17 A. Godeke, B. ten Haken, H. H. J. ten Kate, and D. C. Larbalestier, A general scaling relation for the critical current density in Nb_3Sn, Supercond. Sci. Technol. **19**, R100 (2006).
18 W. D. Markiewicz, Elastic stiffness model for the critical temperature Tc of Nb_3Sn including strain dependence, Cryogenics **44**, 767 (2004).
19 W. D. Markiewicz, Invariant temperature and field strain functions for Nb_3Sn composite superconductors, Cryogenics **46**, 846 (2006).
20 R. Zhang, P. Gao, and X. Wang, Strain dependence of critical superconducting properties of Nb_3Sn with different intrinsic strains based on a semi-phenomenological approach, Cryogenics **86**, 30 (2017).
21 J. W. Ekin, Unified scaling law for flux pinning in practical superconductors: I. Separability postulate, raw scaling data and parameterization at moderate strains, Supercond. Sci. Technol. **23**, 083001 (2010).
22 J. W. Ekin, N. Cheggour, L. Goodrich, J. Splett, B. Bordini, and D. Richter, Unified scaling law for flux pinning in practical superconductors: II. Parameter testing, scaling constants, and the extrapolative scaling expression, Supercond. Sci. Technol. **29**, 123002 (2016).
23 J. W. Ekin, N. Cheggour, L. Goodrich, and J. Splett, Unified Scaling Law for flux pinning in practical superconductors: III. Minimum datasets, core parameters, and application of the extrapolative scaling expression, Supercond. Sci. Technol. **30**, 033005 (2017).
24 D. P. Boso, M. Lefik, and B. A. Schrefler, Homogenisation methods for the thermo-mechanical analysis of Nb_3Sn strand, Cryogenics **46**, 569 (2006).
25 J. Chen, K. Han, and P. N. Kalu, 3D stress-strain model of the Nb_3Sn wire, IEEE Trans. Appl. Supercond. **21**, 2509 (2011).
26 E. Q. Sun, Multi-scale nonlinear stress analysis of Nb_3Sn superconducting accelerator magnets, Supercond. Sci. Technol. **35**, 045019 (2022).
27 Y. Feng, H. Yong, and Y. Zhou, Efficient multiscale investigation of mechanical behavior in Nb_3Sn superconducting accelerator magnet based on self-consistent clustering analysis, Compos. Struct. **324**, 117541 (2023).
28 K. Osamura, S. Machiya, Y. Tsuchiya, H. Suzuki, T. Shobu, M. Sato, T. Hemmi, Y. Nunoya, and S. Ochiai, Local strain and its influence on mechanical-electromagnetic properties of twisted and untwisted ITER Nb_3Sn strands, Supercond. Sci. Technol. **25**, 054010 (2012).
29 M. Ahoranta, J. Lehtonen, and T. Tarhasaari, Modelling the effect of twisting on electro-mechanical properties of Nb_3Sn conductors, Cryogenics **49**, 694 (2009).
30 Z. Jing, H. Yong, and Y. Zhou, Theoretical modeling for the effect of twisting on the properties of multifilamentary Nb_3Sn superconducting strand, IEEE Trans. Appl. Supercond. **23**, 6000307 (2013).
31 B. Liu, Z. Jing, H. Yong, and Y. Zhou, Strain distributions in superconducting strands with twisted filaments, Compos. Struct. **174**, 158 (2017).
32 D. M. J. Taylor, S. A. Keys, and D. P. Hampshire, Reversible and irreversible effects of strain on the critical current density of a niobium-tin superconducting wire, Cryogenics **42**, 109 (2002).
33 L. F. Goodrich, N. Cheggour, X. F. Lu, J. D. Splett, T. C. Stauffer, and B. J. Filla, Method for determining the irreversible strain limit of Nb_3Sn wires, Supercond. Sci. Technol. **24**, 075022 (2011).
34 N. Cheggour, T. C. Stauffer, W. Starch, P. J. Lee, J. D. Splett, L. F. Goodrich, and A. K. Ghosh, Precipitous change of the irreversible strain limit with heat-treatment temperature in Nb_3Sn wires made by the restacked-rod process, Sci. Rep. **8**, 13048 (2018).
35 N. Cheggour, T. C. Stauffer, W. Starch, L. F. Goodrich, and J. D. Splett, Implications of the strain irreversibility cliff on the fabrication of particle-accelerator magnets made of restacked-rod-process Nb_3Sn wires, Sci. Rep. **9**, 5466 (2019).
36 X. Wang, Y. Gao, and Y. Zhou, Electro-mechanical behaviors of composite superconducting strand with filament breakage, Physica C **529**, 26 (2016).
37 X. Wang, Y. Li, and Y. Gao, Mechanical behaviors of multi-filament twist superconducting strand under tensile and cyclic loading, Cryogenics **73**, 14 (2016).
38 L. Jiang, X. Su, L. Shen, J. Zhou, and X. Zhang, Damage behavior of Nb_3Sn/Cu superconducting strand at room temperature under asymmetric strain cycling, Fusion Eng. Des. **172**, 112869 (2021).
39 L. Jiang, X. Zhang, and Y. H. Zhou, Nonlinear static and dynamic mechanical behaviors of Nb_3Sn superconducting composite wire: Experiment and analysis, Acta Mech. Sin. **39**, 122322 (2023).
40 T. Mura, Micromechanics of Defects in Solids (Springer Netherlands, Dordrecht, 1987).
41 G. L. Shen, G. K. Hu, and B. Liu, Mechanics of Composite Materials (Tsinghua University Press, Beijing, 2013).
42 T. Mori, and K. Tanaka, Average stress in matrix and average elastic energy of materials with misfitting inclusions, Acta Metall. **21**, 571 (1973).
43 J. D. Eshelby, The determination of the elastic field of an ellipsoidal inclusion, and related problems, Royal Society, **241**, 376 (1957).
44 I. Doghri, Mechanics of Deformable Solids (Springer, Berlin, Heidelberg, 2000).
45 I. Doghri, and A. Ouaar, Homogenization of two-phase elasto-plastic composite materials and structures, Int. J. Solids Struct. **40**, 1681 (2003).
46 J. Mazars, and G. Pijaudier-Cabot, Continuum damage theory—Application to concrete, J. Eng. Mech. **115**, 345 (1989).
47 S. Murakami, Continuum Damage Mechanics (Springer Netherlands, Dordrecht, 2012).
48 W. L. Azoti, A. Tchalla, Y. Koutsawa, A. Makradi, G. Rauchs, S. Belouettar, and H. Zahrouni, Mean-field constitutive modeling of elasto-plastic composites using two (2) incremental formulations, Compos. Struct. **105**, 256 (2013).
49 A. Tchalla, W. L. Azoti, Y. Koutsawa, A. Makradi, S. Belouettar, and H. Zahrouni, Incremental mean-fields micromechanics scheme for non-linear response of ductile damaged composite materials, Compos. Part B-Eng. **69**, 169 (2015).

50 E. Barzi, G. Ambrosio, N. Andreev, R. Bossert, R. Carcagno, S. Feher, V. S. Kashikhin, V. V. Kashikhin, M. J. Lamm, F. Nobrega, I. Novitski, Y. Pishalnikov, C. Sylvester, M. Tartaglia, D. Turrioni, R. Yamada, A. V. Zlobin, M. Field, S. Hong, J. Parrell, and Y. Zhang, Performance of Nb_3Sn RRP strands and cables based on a 108/127 stack design, IEEE Trans. Appl. Supercond. **17**, 2718 (2007).

51 N. Mitchell, Finite element simulations of elasto-plastic processes in Nb_3Sn strands, Cryogenics **45**, 501 (2005).

多芯绞扭Nb_3Sn超导股线弹塑性损伤和临界电流不可逆退化的细观力学建模

景泽, 张雨

摘要 Nb_3Sn被广泛接受是实现高场超导磁体的关键材料. 然而, Nb_3Sn是脆性材料且其超导性能具有应变敏感性. 在强磁场应用中, Nb_3Sn股线会受到显著的弹塑性应变甚至损伤, 导致其载流能力下降. 本文基于细观力学方法建立了三维平均场均匀化模型, 研究多芯绞扭Nb_3Sn超导股线的弹塑性损伤行为和临界电流的不可逆退化. 计算股线在单调和循环载荷作用下的等效应力-应变曲线以及Nb_3Sn内部的应变分布. 采用辅以损伤引起退化的应变不变量标度律来表征临界电流的不可逆退化. 研究发现, 绞扭对股线弹塑性损伤行为和应变导致的临界电流退化起着重要作用. 随着绞扭节距的增大, 复合股线的刚度增大, 应变极限(超过该极限时芯丝开始损伤)急剧减小. 累积残余应变和芯丝的损伤共同导致超导股线临界电流的不可逆退化. 实验观察到的“断崖式不可逆退化”是由于Nb_3Sn芯丝的损伤造成的. 从力学的角度, 短绞节距是缓解应变引起超导股线临界电流不可逆退化的良好选择.